Computational Materials Science 244 (2024) 113278

Contents lists available at ScienceDirect

Computational Materials Science

journal homepage: www.elsevier.com/locate/commatsci

Full length article

Theoretical and molecular dynamics studies of critical resolved shear stress for rhombohedral twinning of sapphire

Dalei Xi [a], Yiyang Du [a], Aditya Nagaraj [b], Suk Bum Kwon [b], Dae Nyoung Kim [b], Sangkee Min [b], Woo Kyun Kim [a,*]

[a] *Department of Mechanical and Materials Engineering, University of Cincinnati, Cincinnati, OH 45221, USA*
[b] *Department of Mechanical Engineering, University of Wisconsin-Madison, 1513 University Avenue, Madison, WI 53706, USA*

ARTICLE INFO

Keywords:
Sapphire
Rhombohedral twinning
Critical resolved shear stress (CRSS)
Molecular dynamics simulation

ABSTRACT

Single crystalline sapphire (α-Al_2O_3) possesses superior mechanical, thermal, chemical, and optical properties over a wide range of temperatures and pressure conditions, allowing it for a broad spectrum of industrial applications. For the past few decades, research has aimed at comprehensive understanding of its plastic deformation mechanisms under mechanical loading. In this study, we have employed molecular dynamics (MD) simulations to study rhombohedral twinning of sapphire, which is of critical importance in understanding the plastic deformation of sapphire as one of most commonly observed deformation modes. Since the critical resolved shear stress (CRSS) plays a pivotal role in describing the activation of slip systems, it is adopted in this study as the key parameter for analysis. The CRSS is calculated during the uniaxial compression test of a cubic sapphire crystal, oriented to exclusively activate rhombohedral twinning deformation, under simulation conditions such as temperature, strain rate, and system size. Furthermore, a theoretical model of CRSS is constructed based on theories of thermal activation processes, then empirically fitted to CRSS data gathered from the MD simulations. This model accurately captures the relationships between CRSS and external parameters including temperature, strain rate, and system size and shows excellent agreements with the simulation results.

1. Introduction

Sapphire is a crystalline phase of aluminum oxide (α-Al_2O_3) with high hardness, strong thermal and chemical stability, and excellent optical transparency [1]. Because of these superior properties, sapphire has become one of the most popular substrate materials for applications including light-emitting diodes (LEDs), laser diodes, radiation detectors, screen materials in infrared military equipment and satellite space technology [2–4].

Although sapphire is inherently brittle, it can be plastically deformed under certain conditions, which has been utilized in many applications of sapphire. For example, plastic deformation plays a key role in ductile-regime machining [5] and it is also related to crack formation leading to material failure [6]. Under certain conditions, plastic deformation modes in sapphire can interfere with each other, acting as obstacles for the propagation of deformation and thus hardening the material and enhancing its mechanical properties [7]. Therefore, in order to efficiently utilize sapphire in practice, it is of critical importance to achieve a comprehensive understanding of its plastic deformation mechanisms.

Dislocation slip and twinning are the two most important mechanisms of plastic deformation of crystalline materials, which can occur along a particular crystallographic direction (slip direction) on a particular crystallographic plane (slip plane). This combination of slip direction and slip plane defines a slip system of a crystal. Sapphire, belonging to space group R$\bar{3}$C, has a variety of plastic deformation modes associated with particular slip systems such as basal slip, prismatic slip, pyramidal slip, rhombohedral twinning and so on [1].

One of the most important material properties in understanding the plastic deformation of a crystal is the critical resolved shear stress (CRSS), which is defined as the shear stress component required to activate an event (dislocation slip or twinning) in a slip system. Many experimental studies have investigated the plastic deformation mechanisms of sapphire and measured the CRSS of different slip systems. Bulk compression test has been one of the most common methods to study the plastic deformation of sapphire and measure the CRSS. For example,

---

[*] Corresponding author.

E-mail addresses: xidi@mail.uc.edu (D. Xi), duy4@mail.uc.edu (Y. Du), anagaraj2@wisc.edu (A. Nagaraj), kwon47@wisc.edu (S.B. Kwon), dkim658@wisc.edu (D.N. Kim), sangkee.min@wisc.edu (S. Min), kimwu@ucmail.uc.edu (W.K. Kim).

https://doi.org/10.1016/j.commatsci.2024.113278
Received 31 May 2024; Received in revised form 30 July 2024; Accepted 31 July 2024

Lageröf et al. [8] and Castaing et al. [9] conducted compression experiments on sapphire along various crystallographic directions under the hydrostatic pressure condition to prevent brittle fracture. Both basal and prismatic dislocations were observed from these tests and the CRSS of each slip system was calculated at the temperatures ranging from 200 °C to 1800 °C. According to these experimental results, prismatic slip was activated more easily at temperatures lower than 600 °C while basal slip became more dominant as the temperature increased. They also found that the CRSS of both basal and prismatic slips exhibited strong temperature dependence. Choi et al. [10] and Scott et al. [11] also conducted the bulk compression tests of sapphire on C-plane at temperatures ranging from 1760 °C to 1875 °C. Both experiments reported that rhombohedral twinning was the most dominant deformation mode in the c-axis compression, especially when the temperature is higher than 1100 °C. Not only did the CRSS of rhombohedral twinning obtained from these tests depend on temperature, but it also exhibited the dependence on loading stress. Another type of test to measure the CRSS is the uniaxial tensile loading. Tressler et al. conducted a tensile test on the sapphire filament at temperatures ranging from 1775 °C to 1875 °C and observed dominant slip on the $\{10\bar{1}1\}$ planes. They also measured the corresponding CRSS [12].

Furthermore, theoretical efforts have been made regarding the critical shear stress. Mitchell et al. developed a double kink dislocation model to study the mechanism of basal and prismatic slip of oxides and intermetallics including sapphire, which calculated the corresponding yield stress of different dislocation modes and investigated the temperature dependence of the yield stress [13]. A theoretical model introduced by Nowak et al. [14,15] used effective resolved shear stress to estimate the CRSS of slip and twinning systems during the earliest stages of plasticity induced by nano-indentation, which showed a good agreement between experiments and finite elemental analysis [16].

Besides experimental and theoretical approaches, atomistic computer simulations such as molecular dynamics (MD) are also suitable tools to investigate the plastic deformation of sapphire because these simulations can unveil the fundamental mechanisms of the material system at atomic levels. Many studies have applied MD to investigate the material properties and the deformation mechanisms of sapphire. For example, Wunderlich et al. used MD to study the crack propagation process in sapphire and calculated the fracture toughness [17] and Chang et al. studied the core structure of pyramidal dislocations of sapphire with the application of MD simulations [18]. Moreover, the nucleation of rhombohedral twinning of sapphire was observed in MD simulations by Kuksin et al. under shock wave loading [19]. Recent MD studies on nano-scale machining processes on sapphire such as cutting [20], nano indentations and scratching [21,22] also observed the activation and propagation of multiple plastic deformation systems during machining. MD simulations of nano indentation on C-plane of sapphire applied by Lin et al. observed the activation of basal, prismatic, pyramidal and rhombohedral slip systems during the indentation and investigated the change in surface morphology related to these slip systems [23]. Tochigi et al. studied rhombohedral twinning mechanism with in situ TEM nanoindentation experiments and MD simulations and revealed an atomic shuffling mechanism to be the elementary process of the rhombohedral twinning in sapphire [24]. Qiu et al. conducted MD nano indentation simulations on C-plane of sapphire with Berkovich indenter orientated in two different directions to measure the nano-hardness of sapphire, which revealed the effect of different indenter orientations [25]. MD nano indentation simulations on four crystallographic planes of sapphire were conducted by Xu et al. and the simulation results showed the activation of different slip systems [26].

Among many plastic deformation mechanisms of sapphire, rhombohedral twinning that occurs on the slip system family of $\{1\bar{1}02\}/\langle\bar{1}101\rangle$ has been commonly observed in various experiments [7,8,11,27–29]. As pointed out by Wang et al. [30], plastic deformation in the rhombohedral planes occurs in a wide range of crystallographic orientations as all the samples tested in the paper, including A-plane, C-plane, M-plane, and R-plane of sapphire, resulted in activation of the rhombohedral system while the other slip systems occurred only in a few orientations. Moreover, it was the only activated system for C-plane sapphire [30,31]. In addition, recent experimental studies [31–33] reported on fracture profiles oriented closely along the R-planes of sapphire under various loading conditions. It was suggested that the activation of rhombohedral twinning occurs before dissociation fracture, which promoted crack propagation in the twinning plane. As the rhombohedral twinning system plays an important role in both the plastic deformation behavior and the fracture behavior of sapphire, further understanding of this mechanism is critical to advancing the material's applications in high-precision industries. It is also known that the activation of rhombohedral twinning exhibits a strong temperature dependence [8,16,28,29]. While a phenomenological description of this behavior exists such as Schmid's empirical formula [34], to our knowledge there is no literature reporting an underlying physics-based model that relates CRSS to key experimental parameters such as strain rate, temperature, system size, and so on. In the present study, we carried out MD simulations of the compression test to investigate the rhombohedral twinning of sapphire and calculated the corresponding critical resolved stress by varying parameter values such as temperature, size, and strain rate. A theoretical model based on the rate theory and the thermal activation was also developed and used to understand the relationships between the CRSS and these parameters. The model predictions aligned closely with the simulation outcomes.

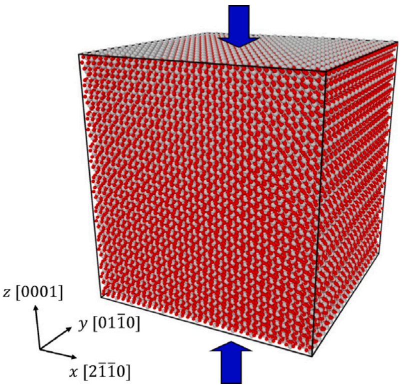

Fig. 1. An atomistic simulation model for the compression test. The arrows indicate the direction of compression.

This article is structured as follows. Section 2 explains the simulation model and methods employed to carry out the compression simulations. Section 3 describes the thermal activation model to predict the CRSS of rhombohedral twinning in sapphire. Simulation results and validation of the model are presented in Section 4. Finally, Section 5 presents the summary of the conclusions.

2. Simulation model and methods

In this study, we performed molecular dynamics simulations of the compression test using LAMMPS (Large-scale Atomistic/Molecular Massively Parallel Simulator) [35]. As shown in Fig. 1, the simulation model is a cubic crystal, oriented to exclusively activate rhombohedral twinning upon compression, i.e., in this orientation the three equivalent slip systems for rhombohedral twinning ($(\bar{1}012)[10\bar{1}1]$, $(1\bar{1}02)[\bar{1}101]$, $(01\bar{1}2)[0\bar{1}11]$) have the largest Schmid factor of 0.45 among all possible slip systems of sapphire. Periodic boundary conditions were applied in all three directions to remove the free surface effect which is otherwise exaggerated due to the large surface-to-volume ratio of atomistic simulation models.

Each model was first fully-equilibrated for 100 ps at a constant temperature using Langevin thermostat [36]. The size of the simulation box was determined by considering the thermal expansion at a given temperature to ensure that the system is in a stress-free state when compression begins. The considered temperatures range from 100 K to 1600 K at an interval of 100 K. During the compression test, the box dimension in the z direction is continuously decreased at a constant strain rate while the x and y dimensions are allowed to independently expand according to the zero stress. The temperature control was stopped once the compression started to prevent artificial influence of thermostat forces from intervening in the physical process. However, even without applying thermostats, the temperature rises only marginally ($\lesssim 2\%$) until a slip event occurs so that the system can still be roughly regarded as in the constant temperature condition. Once a slip is triggered, there occurs a sudden rise in temperature because part of the potential energy is released in the form of the kinetic energy. To see the strain rate effect, three different strain rates of 10^6 s^{-1}, 10^7 s^{-1}, 10^8 s^{-1} were considered. We also tested three different sizes of models including 15,840, 120,960, 967,680 atoms roughly corresponding to the side length of the cubic box of 50 Å, 100 Å, and 200 Å, respectively.

For the interactions between atoms, Vashishta potential was employed [37]. This interatomic potential is known for its capability of properly predicting elastic constants, cohesive energy, bulk modulus, melting temperature, and so on. It also showed great consistency in the description of plastic deformations in our previous studies [20,21, 38,39]. All the simulations were repeated 5 times by assigning different initial velocities and equilibrating with different random seed numbers in Langevin thermostat. The analysis of the simulation results was carried out using the Open Visualization Tool (OVITO) [40].

3. Construction of the thermal activation model for CRSS prediction

Here we focus on developing a theoretical model that can predict the CRSS for rhombohedral twinning with three parameters of temperature, system size, and strain rate. This model is based on the thermally-activated transition between states separated by time-varying energy barriers, which has been applied to various areas including chemical reaction, friction, dislocation nucleation, nanoindentation, and so on [41–46]. In the current system, the transition occurs from a defect-free state to a state with twinning activated.

We first develop a model for a single activation site by defining two probability functions $f_1(t)$ and $g_1(t)$. $f_1(t)$ is the cumulative probability of no twinning occurring until time t and therefore gradually decreases from 1 at $t = 0$ approaching zero as t goes to infinity. $g_1(t)$ denotes the probability of twinning occurring at time t, which is related to $f_1(t)$ according to the following equation.

$$g_1(t) = -\frac{d f_1(t)}{dt}. \tag{1}$$

As such, we assume the following rate equation for f_1:

$$\frac{d f_1}{dt} = -k_1 f_1, \tag{2}$$

where k_1 is the transition rate, which can be expressed with the activation energy barrier ΔE between the two states as

$$k_1 = \nu_0 \exp\left(-\frac{\Delta E}{k_{\mathrm{B}} T}\right), \tag{3}$$

where ν_0 is the attempt frequency, k_{B} is the Boltzmann constant, and T denotes the absolute temperature. The activation energy barrier ΔE is a function of the resolved shear stress τ for rhombohedral twinning, i.e., $\Delta E = \Delta E(\tau)$, and τ is a function of the applied compressive strain ε, i.e., $\tau = \tau(\varepsilon)$. During the compression, a constant strain rate of $\dot{\varepsilon}$ is applied so that the compressive strain ε increases as $\varepsilon = \dot{\varepsilon}\, t$ and thus $\tau = \tau(\dot{\varepsilon}\, t)$. Henceforth, we adopt a sign convention for ε such that it is expressed as a positive quantity when compressed. Since there is a one-to-one relation between τ and ε, there also exists a one-to-one relation between τ and time t and

$$\frac{d\tau}{dt} = \frac{d\tau}{d\varepsilon}\frac{d\varepsilon}{dt} = G\dot{\varepsilon}, \tag{4}$$

where G $(= \frac{d\tau}{d\varepsilon})$ is an elastic constant. Thus, both f_1 and g_1 can be written as functions of τ, i.e., $f_1(\tau)$ and $g_1(\tau)$.

In principle, since the event is a probabilistic process, τ_{CRSS} can be defined as an averaged quantity as

$$\tau_{\mathrm{CRSS}} = \int_0^\infty \tau\, g_1(\tau) d\tau. \tag{5}$$

However, assuming a narrow distribution of $g_1(\tau)$ with a single peak (evidenced from the simulation results as will be seen in Section 4.3), τ_{CRSS} can be approximated as τ_{peak}, where g_1 has the maximum, i.e.,

$$\left.\frac{dg_1}{d\tau}\right|_{\tau=\tau_{\mathrm{peak}}} = \frac{1}{G\dot{\varepsilon}}\frac{dg_1}{dt} = 0, \tag{6}$$

which is equivalent to

$$\frac{dg_1}{dt} = -\frac{d^2 f_1}{dt^2} = 0 \tag{7}$$

and, using Eq. (2),

$$k_1^2 = \frac{dk_1}{dt}. \tag{8}$$

A real system contains more than one activation site, each of which can trigger twinning. Similar to the discussion above, two probability functions f_n and g_n can be defined, where n is the number of activation sites. Assuming all activation sites are independent and equivalent, they can be related with f_1 and g_1 as

$$f_n = \prod_{i=1}^{n} f_1 = f_1^{\,n}, \tag{9}$$

$$g_n = -\frac{d f_n}{dt} = -n f_1^{\,n-1}\frac{d f_1}{dt} = n f_1^{\,n-1} g_1. \tag{10}$$

The rate equation for f_n is

$$\frac{d f_n}{dt} = -k_n f_n, \tag{11}$$

where k_n is the transition rate for a system with n activation sites. Since

$$\frac{d f_n}{dt} = \frac{d f_1^n}{dt} = n f_1^{\,n-1}\frac{d f_1}{dt} = n f_1^{\,n-1}(-k_1 f_1) = -n k_1 f_1^n = -n k_1 f_n, \tag{12}$$

$k_n = n k_1$, i.e., the transition rate of the system with n sites is n times larger than that of the single site case. Similar to Eq. (8), the maximum probability condition leads to

$$k_n^2 = \frac{dk_n}{dt}, \tag{13}$$

which is equivalent to

$$n\, k_1^2 = \frac{dk_1}{dt}. \tag{14}$$

Combined with Eq. (3) and assuming $n = sN$, where s is a proportionality constant and N is the number of atoms in the system, the following derivation can be made.

$$\begin{aligned}
sN\left[\nu_0 \exp\left(-\frac{\Delta E}{k_{\mathrm{B}}T}\right)\right]^2 &= -\frac{1}{k_{\mathrm{B}}T}\frac{d\Delta E}{dt}\nu_0 \exp\left(-\frac{\Delta E}{k_{\mathrm{B}}T}\right),\\
sN\,\nu_0 \exp\left(-\frac{\Delta E}{k_{\mathrm{B}}T}\right) &= -\frac{1}{k_{\mathrm{B}}T}\frac{d\Delta E}{dt},\\
\exp\left(-\frac{\Delta E}{k_{\mathrm{B}}T}\right) &= -\frac{G\dot{\varepsilon}}{sN\,\nu_0 k_{\mathrm{B}}T}\frac{d\Delta E}{d\tau},\\
-\frac{\Delta E}{k_{\mathrm{B}}T} &= \ln\left[-\frac{G\dot{\varepsilon}}{sN\,\nu_0\,k_{\mathrm{B}}T}\frac{d\Delta E}{d\tau}\right],
\end{aligned} \tag{15}$$

which can also be written as

$$-\frac{1}{T}\left(\frac{\Delta E}{k_{\mathrm{B}}}\right) = \ln A + \ln\left[\frac{\dot{\varepsilon}}{NT}\right] + \ln\left[-\frac{d}{d\tau}\left(\frac{\Delta E}{k_{\mathrm{B}}}\right)\right], \tag{16}$$

where $A = \frac{G}{s\nu_0}$ and is used as a fitting constant. Eq. (16) can be solved for $\tau_{\mathrm{CRSS}} = \tau_{\mathrm{CRSS}}(\dot{\varepsilon}, N, T)$ once $\Delta E(\tau)$ is known.

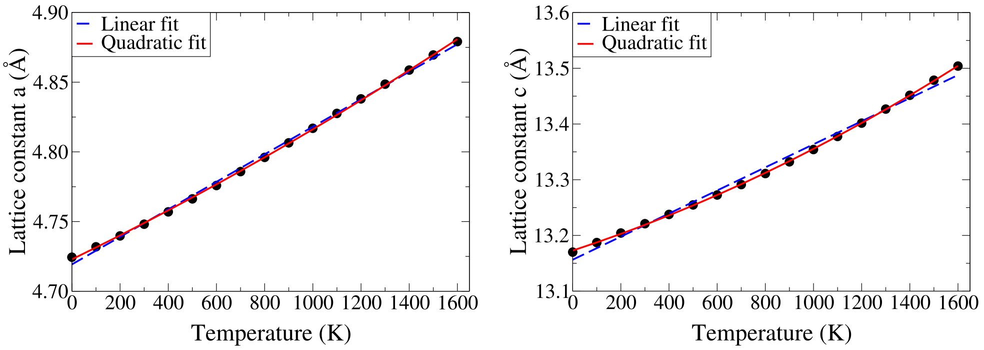

(a) Lattice constant a

(b) Lattice constant c

Fig. 2. Temperature-dependent lattice constants a and c between 0 K and 1600 K. In each graph, the blue dashed line and the red solid line show the linear and quadratic fits, respectively.

Based on the simulation results showing a transitional behavior at about 450 K (See Fig. 7(a)), we used two functional forms for $\Delta E(\tau)$. For the low-temperature cases (below 450 K) where the transition can occur only when ΔE is substantially reduced, the following form was used:

$$\frac{\Delta E}{k_{\mathrm{B}}} = \lambda_{\mathrm{low}} \left(\tau_{\max} - \tau\right)^{m}, \tag{17}$$

where $\tau_{\max}$ is the maximum resolved shear stress where ΔE completely vanishes. It is also known that $m = 3/2$ as τ approaches $\tau_{\max}$ [47]. Thus, in this regime of low temperature, we have three fitting constants A_{low}, λ_{low}, $\tau_{\max}$. The solution to Eq. (16) with Eq. (17) is given by

$$\tau_{\mathrm{CRSS}}^{\mathrm{low}} = \tau_{\max} - \exp\left[-\frac{c_2}{c_1} - \frac{1}{m} W_0\left(\frac{m}{c_1}\exp\left(-\frac{c_2}{c_1}m\right)\right)\right], \tag{18}$$

where W_0 is the principal branch of the Lambert W function (i.e., the inverse function of $y = xe^{x}$) and

$$c_1 = \frac{T(m-1)}{\lambda_{\mathrm{low}}}, \tag{19}$$

$$c_2 = \frac{T}{\lambda_{\mathrm{low}}}\left(\ln A + \ln\left[\frac{m\lambda_{\mathrm{low}}\dot{\varepsilon}}{NT}\right]\right). \tag{20}$$

For the high-temperature cases (above 450 K), a power function was used as

$$\frac{\Delta E}{k_{\mathrm{B}}} = \frac{\lambda_{\mathrm{high}}}{\tau^{p}}. \tag{21}$$

Then, the solution to Eq. (16) is

$$\tau_{\mathrm{CRSS}}^{\mathrm{high}} = \exp\left[\frac{c_4}{c_3} + \frac{1}{p} W_0\left(\frac{p}{c_3}\exp\left(-\frac{c_4}{c_3}p\right)\right)\right], \tag{22}$$

where

$$c_3 = \frac{T(p+1)}{\lambda_{\mathrm{high}}}, \tag{23}$$

$$c_4 = \frac{T}{\lambda_{\mathrm{high}}}\left(\ln A + \ln\left[\frac{p\lambda_{\mathrm{high}}\dot{\varepsilon}}{NT}\right]\right). \tag{24}$$

The three fitting parameters of the high temperature model are A_{high}, λ_{high} and the exponent p.

4. Results and discussion

4.1. Thermal expansion

We first calculated the equilibrium lattice constants a and c of sapphire at temperatures ranging from 0 K to 1600 K. The results are shown in Fig. 2. The 0 K constants were determined by performing energy minimization simultaneously allowing simulation box relaxation according to zero pressure. The finite temperature lattice constants were obtained from the constant pressure and constant temperature simulations with zero applied pressure. The values shown in the graphs are averaged over a time length of 80 ps and the graphs also show the linear and quadratic fitting results. Overall, the quadratic fit describes the temperature dependence better than the linear fit for both lattice constants.

The lattice constants at 300 K were calculated as $a = 4.748$ Å and $c = 13.221$ Å exhibiting only 0.233% and 1.77% deviations from the experimental values at 295.65 K, which are $a = 4.759$ Å and $c = 12.992$ Å, respectively [1]. Also, the 300 K thermal expansion coefficients for a and c were calculated as 1.819×10^{-5} K^{-1} and 1.262×10^{-5} K^{-1}, respectively, which somewhat overestimate the experimental values of 5.0×10^{-6} K^{-1} for a and 6.6×10^{-6} K^{-1} for c in the range of 293 K and 323 K [1].

4.2. Sapphire deformation during compression

During the compression test, only rhombohedral twinning deformation was observed in one of the three equivalent R-planes as discussed in Section 2. A typical twinning process is illustrated in Fig. 3, where atoms are colored according to the atomic strain, which is calculated by

$$\sqrt{E_{xy}^2 + E_{yz}^2 + E_{zx}^2 + \frac{1}{6}\left[(E_{xx} - E_{yy})^2 + (E_{yy} - E_{zz})^2 + (E_{zz} - E_{xx})^2\right]} \tag{25}$$

where E_{ij} is the component of Lagrange strain tensor, calculated using the method in Ref. [48]. When the strain reaches 0.13302, a twinning event develops at a local site as shown in Fig. 3(b). Fig. 3(c) shows that this twinning deformation propagates in R-plane making a twin region (i.e. a rhombohedral twin). Eventually, several twins are formed as the compressive strain further increases as shown in Fig. 3(d).

Magnified images showing the detailed atomic configurations before and after rhombohedral twinning are shown in Fig. 4. All the atoms in Fig. 4(a) are colored differently but in the undeformed configuration. Blue atoms bounded with the other atoms in the $(01\bar{1}2)$ plane form a twin after the twinning in the $[0\bar{1}11]$ direction occurs. The red atoms that are in the same vertical position in the undeformed configuration as in Fig. 4(a) experience a fault across the twin (blue region) in the deformed configuration as in Fig. 4(b). The twin structure of the blue atoms in Fig. 4(b) is clearly seen as guided by the dashed lines.

Fig. 5(a) shows the relation between the compressive strain ε and the compressive stress σ_{zz} during the compression simulation for a representative case of the 100 Å-sized model at 1000 K and at a strain rate of 10^{8} s^{-1}. Other models exhibited similar behaviors. As the compressive strain increases, the box dimension in the z direction continuously decreases while the corresponding compressive stress σ_{zz} increases. Note that the box sizes in the x and y directions increase

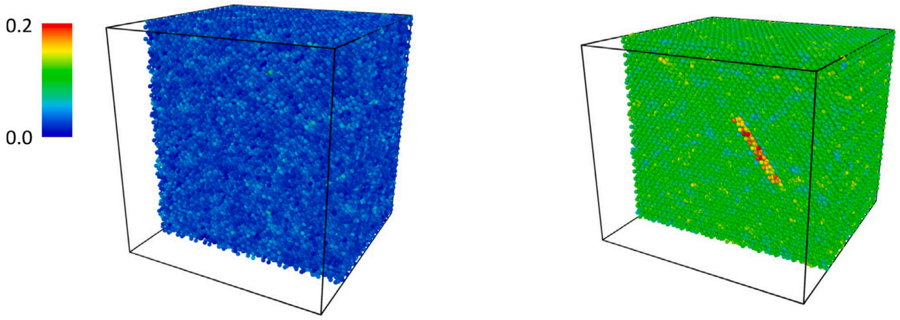

(a) $\varepsilon = 0$ (b) $\varepsilon = 0.13302$

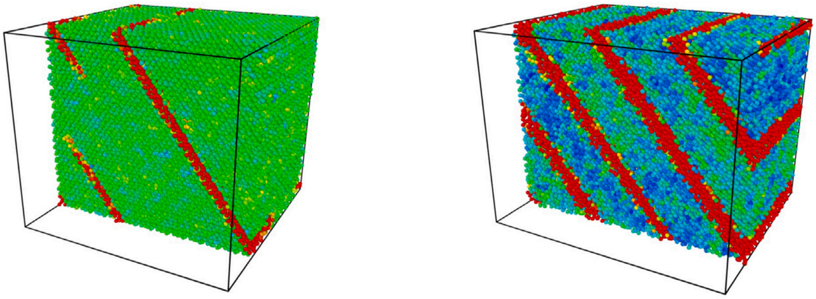

(c) $\varepsilon = 0.13317$ (d) $\varepsilon = 0.13369$

Fig. 3. Rhombohedral twinning develops as the compressive strain ε increases. Atoms are colored according to the atomic strain calculated by Eq. (25).

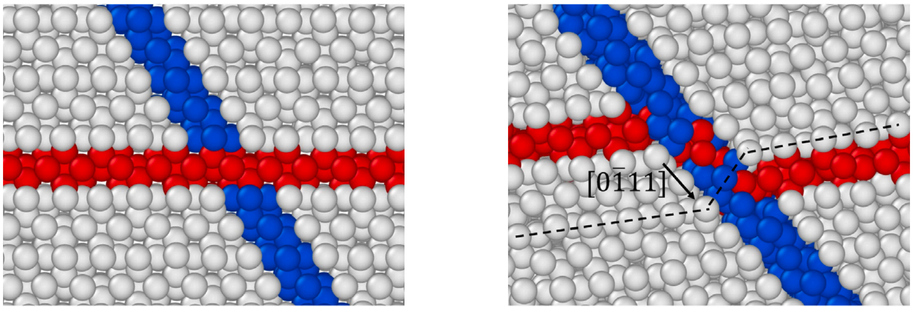

(a) Before twinning (b) After twinning

Fig. 4. Atomic configurations (a) before and (b) after rhombohedral twinning. In (a) all atoms are in the undeformed configuration even though they are colored differently. The blue atoms are bounded with the other atoms in the $(01\bar{1}2)$ plane and those atoms in the same vertical locations in the undeformed configuration are colored red. The dashed lines in (b) are introduced to show the twin structure.

according to the zero pressure condition as the simulation box is compressed in the z direction. The Schmid factor S_d for the slip system responsible for rhombohedral twinning is determined by the relative orientations of the normal vector to the slip plane and the slip vector with respect to the compression direction (z axis). These orientations change as the simulation box deforms. The normal and slip vectors in the deformed simulation box were calculated by applying the deformation gradient of the current box dimensions relative to the original box dimensions. This method was also validated by computing the orientation of atom layers parallel to the slip plane as well as the relative positions of atoms along the slip vector. An example in such changes in Schmid factor S_d is shown in Fig. 5(b). As a combined effect, the corresponding resolved shear stress τ, which is calculated as $\sigma_{zz} \times S_d$, also increases as Fig. 5(c) shows. At a critical strain, the system can no longer maintain the undeformed configuration and a twinning is triggered accompanying an abrupt drop in the stress value. The peak in the resolved shear stress defines the critical resolved shear stress τ_{CRSS} as indicated in Fig. 5(c).

4.3. *Temperature dependence*

As many previous studies have found [8,10,11,16,28,29], temperature plays a significant role in the deformation behavior of sapphire as the atomic-scale plastic deformation mechanisms happen through thermal activation. As seen in Eq. (3), the transition rate in a thermally activated process is dictated as an Arrhenius-type relation with temperature so that it increases as temperature rises for a given energy barrier. As a result, it is expected that the transition (in our case a twinning event) occurs at earlier stages during compression with increasing temperature. Since the critical resolved shear stress τ_{CRSS} is defined as the shear stress when a twinning is triggered, the earlier transition means the lower τ_{CRSS} and thus τ_{CRSS} should decrease as temperature rises. This dependence of τ_{CRSS} on temperature has been observed from our simulation results. Fig. 6 shows the relations between τ and compressive strain ε at four representative temperatures (400 K, 800 K, 1200 K, and 1600 K). As evident from the figure, the sharp drop of τ occurs earlier with increasing temperature, meaning a transition has been initiated.

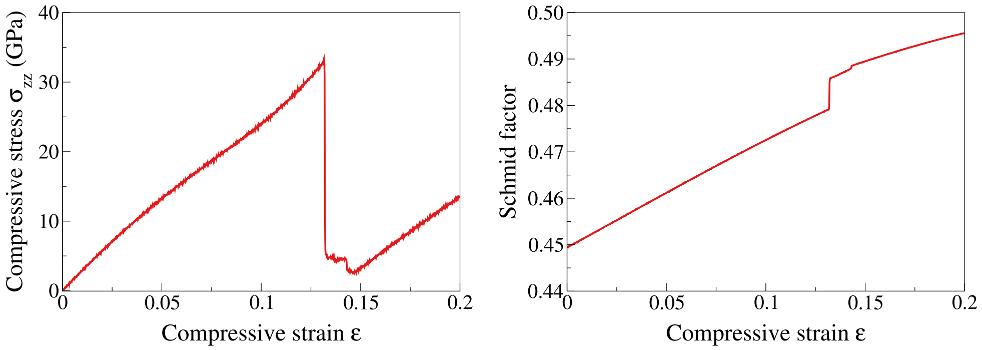

(a) Compressive stress (b) Schmid factor

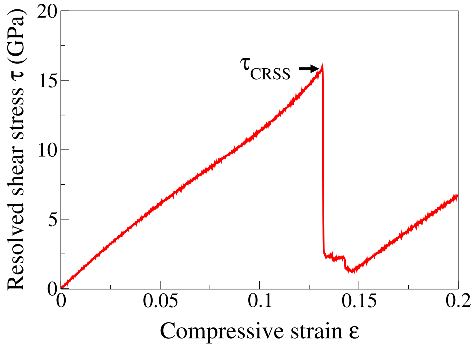

(c) Resolved shear stress

Fig. 5. Typical changes in (a) the compressive stress σ_{zz}, (b) Schmid factor, and (c) the resolved shear stress τ for the rhombohedral twinning system as the compressive strain ε increases. The critical resolved shear stress τ_{CRSS} is defined as the peak force in (c).

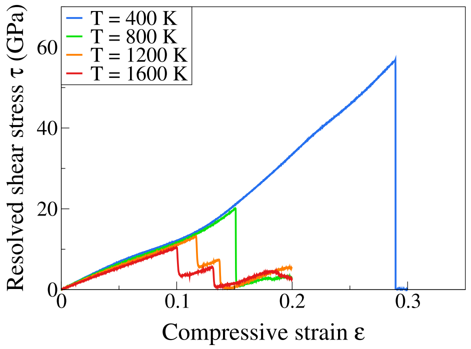

Fig. 6. The resolved shear stress τ as a function of compressive strain ε at four temperatures.

The simulation results are summarized in Fig. 7(a), which shows τ_{CRSS} as a function of temperature for the model with $N = 120{,}960$ and compressed at $\dot{\varepsilon} = 10^8\ \text{s}^{-1}$. Each temperature simulation was repeated five times and the data shown in the graph are the averaged values. The narrow gap between the lower and upper error bars of each data point proves that the transition at each temperature occurs in a very narrow distribution as conjectured in Section 3. The figure also shows a distinction in the behavior of τ_{CRSS} as temperature decreases. Between 500 K and 1600 K, τ_{CRSS} rises more rapidly as temperature decreases. However, after a critical point of about 450 K, the rise of τ_{CRSS} becomes flattened converging a constant value $\tau_{\max}$. This transition in the dependence of temperature is more clearly seen in Fig. 7(b), where τ_{CRSS} is re-scaled as $(\tau_{\max} - \tau_{\text{CRSS}})/\text{T}$. This corrected $(\tau_{\max} - \tau_{\text{CRSS}})/\text{T}$ rapidly increases up to 500 K but after a peak at 600 K it decreases with increasing temperature. These observations justify using two different models for the low-temperature regime and for the high-temperature regime as in Section 3. The solid fitting curves in Fig. 7(a) are constructed using Eq. (18) and Eq. (22), which accurately represent the two sets of data.

The low-temperature fitting parameters were determined using the four lower temperature data at 100 K, 200 K, 300 K, and 400 K in Fig. 7(a) and their values are $A_{\text{low}} = \exp(-2.04572)$ GPa s, $\lambda_{\text{low}} = 0.62181\ \text{GPa}^{-m}$ K, and $\tau_{\max} = 70.961$ GPa. For the high-temperature model fitting, not only all the lower temperature data in Fig. 7(a) (500 K to 1600 K) but also the other data at 1000 K with different numbers of atoms and different strain rates are used. The results of the latter data will be presented in the following section. The parameter values are $A_{\text{high}} = \exp(-34.117)$ GPa s, $\lambda_{\text{high}} = 264{,}291\ \text{GPa}^{p}$ K, and $p = 0.81183$.

4.4. Strain-rate and size dependence

The thermal activation is a probabilistic process so that the longer the waiting time the higher chance for a transition to occur. Thus, if the compression proceeds slowly, i.e., at a lower strain rate, the system will have a higher probability to make a transition before reaching a given strain. Thus, it is expected that τ_{CRSS} will decrease with decreasing strain rate. This dependence on the strain rate is taken into account in our models as seen in Section 3.

The strain-rate dependence was tested with two models of $N = 15{,}840$ and $N = 120{,}960$ at 1000 K. The strain rate varied from $10^6\ \text{s}^{-1}$ to $10^8\ \text{s}^{-1}$. The typical behaviors are shown in Fig. 8(a), presenting the stress–strain results of the model with $N = 120{,}960$. Clearly, as the strain decreases from $10^8\ \text{s}^{-1}$ to $10^6\ \text{s}^{-1}$, the drop in τ occurs at lower strains. As such, the simulations were repeated five times and the averaged data are shown in Fig. 8(b) with the standard errors. The horizontal axis in Fig. 8(b) is logarithmic because the model predicts the logarithmic dependence on strain rate. Both models with $N = 15{,}840$ and $N = 120{,}960$ exhibit the decrease in τ_{CRSS} as the strain rate decreases. The figure also shows the fitting curves calculated using the high-temperature model in Eq. (22). The fitting parameters are

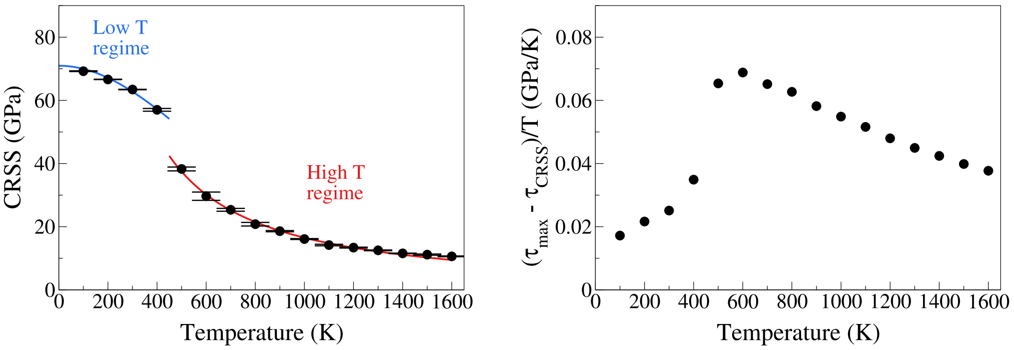

(a) τ_{CRSS} (b) $(\tau_{\max} - \tau_{\mathrm{CRSS}})/\mathrm{T}$

Fig. 7. τ_{CRSS} vs. temperature for the model with N = 120,960 and compressed at $\dot{\varepsilon} = 10^8$ s^{-1}. The dots in (a) are the averaged τ_{CRSS} over the five cases at each temperature and the error bars indicate the standard errors. The solid curves in (a) are obtained using the low-temperature and high-temperature models in Eq. (18) and Eq. (22), respectively. In (b), a re-scaled τ_{CRSS} is presented as $(\tau_{\max} - \tau_{\mathrm{CRSS}})/\mathrm{T}$ to more clearly show a transition in the behavior between 400 K and 500 K.

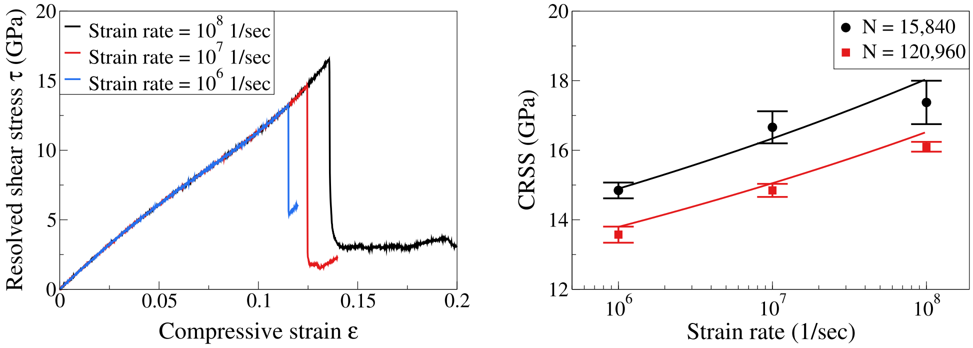

(a) τ_{CRSS} vs. ε (b) τ_{CRSS} vs. strain rate

Fig. 8. The effects of the strain rate on τ_{CRSS}. (a) shows the results of the model with $N = 120,960$ at 1000 K and at three different orders of strain rates. In (b), the data points are the averaged quantities with five simulations for each case and the error bars represent the standard error. The solid lines are the fitting curves based on the high-temperature model in Eq. (22).

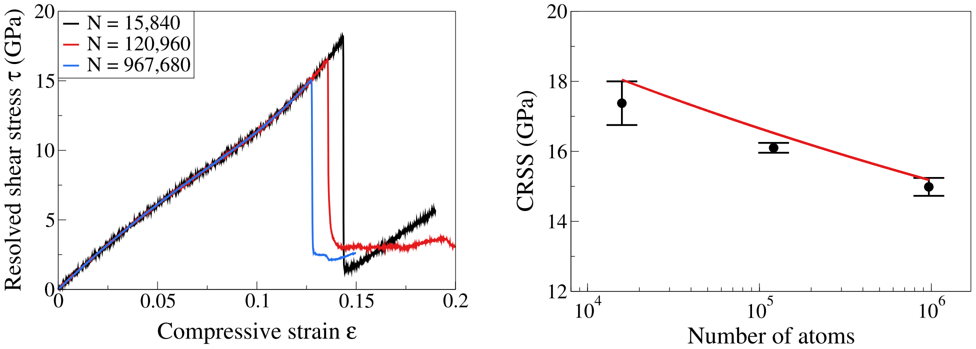

(a) τ_{CRSS} vs. ε (b) τ_{CRSS} vs. number of atoms

Fig. 9. The effects of the system size (number of atoms N) on τ_{CRSS}. (a) shows the results of the model with three different sizes at $\dot{\varepsilon} = 10^8$ s^{-1} and at 1000 K. In (b), the data points are the averaged quantities with five simulations for each case and the error bars represent the standard error. The solid line is the fitting curve based on the high-temperature model in Eq. (22).

identical as used in Fig. 7(a). It is evident that our model predictions exhibit a close agreement with the simulation results.

Our model also predicts a dependence of τ_{CRSS} on the system size because larger systems contain more activation sites than smaller systems and the transition rate with n sites is n times larger than that of the single site model as discussed in Section 3. This size dependence was also tested using the compression simulations. Fig. 9(a) shows the stress–strain relations of the models with different numbers of atoms (N = 15,840, $N = 120,960$, and $N = 967,680$) at 1000 K and at $\dot{\varepsilon} = 10^8$ s^{-1}. As expected, the transition takes place at lower strains as the system size increases. The averaged results from the five repeated simulations are plotted in Fig. 9(b) together with the standard errors. The logarithmic dependence on N is clearly seen in the figure. The high-temperature fitting curve included in the figure clearly represents this trend within the same orders of error as the standard bars indicate.

Moreover, $\dot{\varepsilon}$ and N appear only in a single term combined as $\ln\left[\dot{\varepsilon}/N\right]$ in Eq. (16). Thus, if the model is valid, τ_{CRSS} for various sizes and strain rates should collapse into a single curve when plotted against $\ln\left[\dot{\varepsilon}/N\right]$. Indeed, in Fig. 10 where τ_{CRSS} is plotted against $\dot{\varepsilon}/N$ at 1000 K in the log scale, all the data are represented by a single curve

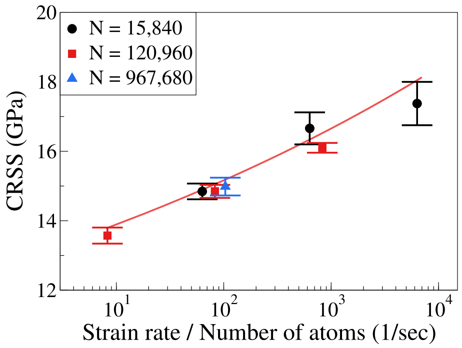

Fig. 10. τ_{CRSS} as a function of $\dot{\varepsilon}/N$ at 1000 K. The data points are colored based on the number of atoms and the error bars represent the standard errors. The solid line is the fitting curve based on the high-temperature model in Eq. (22).

constructed by the high-temperature model using the same parameters as in Figs. 7(a), 8(b), and 9(b) and, therefore, prove the validity of our model.

4.5. Discussion

While the same dependences on temperature and strain rate as we observed with MD simulations have been found in experiments as well [10,11], there are orders of magnitude discrepancy in actual CRSS values between experiments and simulations. As seen in Fig. 7(a), τ_{CRSS} ranged between 10 GPa and 70 GPa in MD simulations, but the typical experimental CRSS for rhombohedral twinning does not exceed 1 GPa even at a room temperature of 295 K [10]. One of the main causes of this discrepancy lies in the huge difference in strain rates. Because of the time-scale limitation of MD simulations, the strain rate for the compression simulation was between 10^6 s^{-1} and 10^8 s^{-1} while typical experimental strain rates range from 10^{-4} s^{-1} to 10^{-6} s^{-1}. Another reason is the incomparable difference in system size. Whereas the largest simulation model that we tested has about 1 million atoms, any macroscopic systems contain astronomical numbers of atoms on the scale of Avogadro's number ($\sim 10^{23}$). As our model predicts, τ_{CRSS} will further decrease if smaller strain rates and bigger models are used in MD simulations. Finally, the real material inevitably contains various forms of defects that are introduced during the manufacturing process. From these defects, slip/twinning deformations can be triggered more easily and thus lower the critical resolved shear stress.

5. Conclusion

In this work, we have examined the activation of rhombohedral twinning in single crystal sapphire using the molecular dynamics simulation method. As the critical resolved shear stress is one of the key parameters dictating the condition for twinning to initiate, it was chosen to be the characterizing parameter of twinning activation within the sapphire system. We conducted uniaxial compression tests in a crystallographic orientation that exclusively activates rhombohedral twinning, due to the system having the highest Schmid factor among all possible slip systems. To examine the relationships between CRSS and external parameters such as temperature, strain rate, and system size, we conducted tests across a temperature range of 100 K to 1600 K (with 100 K interval) and compression strain rates varying between 10^6 s^{-1} and 10^8 s^{-1} for cubic sapphire crystals with side lengths of 50 Å, 100 Å, and 200 Å, each of which contains 15,840, 120,960, 967,680 atoms, respectively. The simulations were performed at a constant strain rate, gradually increasing the resolved shear stress for the slip system responsible for rhombohedral twinning. Once a twinning process was activated, the resolved shear stress exhibited a sharp drop in magnitude such that the critical resolved shear stress was calculated as the peak value for given combinations of conditions.

We also constructed a theoretical model relating CRSS to temperature, strain rate, and system size based on thermally activated events. This model depends on how the activation energy barrier ΔE varies as the applied resolved shear stress τ changes. Since the calculated τ_{CRSS} exhibited two distinctive temperature-dependent behaviors bordered at about 450 K, we assumed two functional forms for ΔE for each temperature regime, i.e, $\Delta E \sim (\tau_{\max} - \tau)^m$ for lower temperatures and $\Delta E \sim \tau^{-p}$ for higher temperatures. The model can properly capture the essential dependence of CRSS on temperature, strain rate, and system size such that it correctly predicts the increase in CRSS with decreasing temperature, increasing strain rate, and decreasing system size and vice versa. Subsequently, the model parameters were determined by fitting them to the calculated CRSS values and the resultant numerical predictions of the model demonstrated excellent agreements with the simulation results over all the tested conditions.

Finally, we provided a discussion about several critical factors causing the discrepancy in CRSS magnitude between MD simulations and experiments such as inherent differences of strain rates and system sizes. Manufacturing defects are considered as another potential cause of this discrepancy.

We believe that the model developed for rhombohedral twinning of sapphire can be universally applied to other plastic deformation modes of any crystalline materials. Thus, applying the model to other systems remains as our future research objectives.

CRediT authorship contribution statement

Dalei Xi: Writing – review & editing, Writing – original draft, Visualization, Validation, Software, Methodology, Investigation, Formal analysis, Data curation, Conceptualization. **Yiyang Du:** Writing – review & editing, Software, Methodology, Investigation, Formal analysis, Data curation. **Aditya Nagaraj:** Writing – review & editing, Validation. **Suk Bum Kwon:** Writing – review & editing, Validation. **Dae Nyoung Kim:** Writing – review & editing, Validation. **Sangkee Min:** Writing – review & editing, Validation, Funding acquisition, Conceptualization. **Woo Kyun Kim:** Writing – review & editing, Writing – original draft, Visualization, Supervision, Software, Resources, Project administration, Methodology, Funding acquisition, Formal analysis, Data curation, Conceptualization.

Declaration of competing interest

The authors declare that they have no known competing financial interests or personal relationships that could have appeared to influence the work reported in this paper.

Data availability

Data will be made available on request.

Acknowledgments

D. Xi, Y. Du, and W. K. Kim at University of Cincinnati were supported in part by the National Science Foundation, United States under Award Number 2009150 and A. Nagaraj, S. B. Kwon, D. N. Kim, S. Min at University of Wisconsin, Madison, were supported in part by the National Science Foundation, United States under Award Number 2008563.

References

[1] E.R. Dobrovinskaya, L.A. Lytvynov, V. Pishchik, Sapphire – Material, Manufacturing, Applications, Springer, 2009.

[2] E. Gu, C.W. Jeon, H. Choi, G. Rice, M. Dawson, E. Illy, M. Knowles, Micromachining and dicing of sapphire, gallium nitride and micro LED devices with UV copper vapour laser, Thin Solid Films (ISSN: 0040-6090) 453–454 (2004) 462–466, http://dx.doi.org/10.1016/j.tsf.2003.11.133, URL https://www.sciencedirect.com/science/article/pii/S0040609003017383.

[3] Z.C. Li, Z.J. Pei, P.D. Funkenbusch, Machining processes for sapphire wafers: a literature review, Proc. Inst. Mech. Eng. B (ISSN: 0954-4054) 225 (7) (2011) 975–989, http://dx.doi.org/10.1177/2041297510393667, URL http://journals.sagepub.com/doi/10.1177/2041297510393667.

[4] G. Katyba, K. Zaytsev, I. Dolganova, I. Shikunova, N. Chernomyrdin, S. Yurchenko, G. Komandin, I. Reshetov, V. Nesvizhevsky, V. Kurlov, Sapphire shaped crystals for waveguiding, sensing and exposure applications, Prog. Cryst. Growth Charact. Mater. (ISSN: 0960-8974) 64 (4) (2018) 133–151, http://dx.doi.org/10.1016/j.pcrysgrow.2018.10.002, URL https://www.sciencedirect.com/science/article/pii/S0960897418300299.

[5] S. Goel, The current understanding on the diamond machining of silicon carbide, J. Phys. D: Appl. Phys. 47 (24) (2014) 243001, http://dx.doi.org/10.1088/0022-3727/47/24/243001.

[6] G.C. Sih, A.J. Ishlinsky, S.T. Mileiko, Plasticity and Failure Behavior of Solids, Springer Dordrecht, 1990.

[7] J. Castaing, A. Muñoz, A.D. Rodriguez, Hardening of rhombohedral twinning in sapphire (α-Al2O3) by basal slip dislocations, Phil. Mag. A 82 (7) (2002) 1419–1431, http://dx.doi.org/10.1080/01418610208235680.

[8] K.P.D. Lageröf, A.H. Heuer, J. Castaing, J.P. Rivière, T.E. Mitchell, Slip and twinning in sapphire (α-Al_2O_3), J. Am. Ceram. Soc. 77 (2) (1994) 385–397, http://dx.doi.org/10.1111/j.1151-2916.1994.tb07006.x, URL https://ceramics.onlinelibrary.wiley.com/doi/abs/10.1111/j.1151-2916.1994.tb07006.x.

[9] G. Castaing, J. Cadoz, S. Kirby, Prismatic slip of Al_2O_3 single crystals below 1000°C in compression under hydrostatic pressure, J. Am. Ceram. Soc. 64 (1981) 504–511.

[10] J.K. Choi, K.H. Auh, Temperature and stress dependence of rhombohedral twinning in sapphire, Mater. Lett. 24 (1995) 161–165, http://dx.doi.org/10.1016/0167-577X(95)00055-0.

[11] W.D. Scott, K.K. Orr, Rhombohedral twinning in alumina, J. Am. Ceram. Soc. 66 (1) (1983) 27–32, http://dx.doi.org/10.1111/j.1151-2916.1983.tb09962.x, URL https://ceramics.onlinelibrary.wiley.com/doi/abs/10.1111/j.1151-2916.1983.tb09962.x.

[12] R.E. Tressler, D.J. Barber, Yielding and flow of c-Axis Sapphire filaments, J. Am. Ceram. Soc. 57 (1) (1974) 13–19, http://dx.doi.org/10.1111/j.1151-2916.1974.tb11353.x, URL https://ceramics.onlinelibrary.wiley.com/doi/abs/10.1111/j.1151-2916.1974.tb11353.x.

[13] T. Mitchell, P. Peralta, J. Hirth, Deformation by a kink mechanism in high temperature materials, Acta Mater. (ISSN: 1359-6454) 47 (13) (1999) 3687–3694, http://dx.doi.org/10.1016/S1359-6454(99)00207-4, URL https://www.sciencedirect.com/science/article/pii/S1359645499002074.

[14] R. Nowak, M. Sakai, The anisotropy of surface deformation of sapphire: Continuous indentation of triangular indenter, Acta Metall. Mater. 42 (1994) 2879–2891, http://dx.doi.org/10.1016/0956-7151(94)90229-1.

[15] R. Nowak, T. Sekino, K. Niihara, Non-linear surface deformation of the 1010 plane of sapphire: Identification of the linear features around spherical impressions, Acta Metall. Mater. 47 (1999) 4329–4338, http://dx.doi.org/10.1016/S1359-6454(99)00316-X.

[16] N. Tymiak, D. Chrobak, W. Gerberich, O. Warren, R. Nowak, Role of competition between slip and twinning in nanoscale deformation of sapphire, Phys. Rev. B 79, http://dx.doi.org/10.1103/PhysRevB.79.174116.

[17] W. Wunderlich, H. Awaji, Molecular dynamics — simulations of the fracture toughness of sapphire, Mater. Des. (ISSN: 0261-3069) 22 (1) (2001) 53–59, http://dx.doi.org/10.1016/S0261-3069(00)00044-3.

[18] J. Chang, C.T. Bodur, A.S. Argon, Pyramidal edge dislocation cores in Sapphire, Philos. Mag. Lett. 83 (11) (2003) 659–666, http://dx.doi.org/10.1080/09500830310001614513.

[19] A. Kuksin, A. Yanilkin, Formation of twins in sapphire under shock wave loading: Atomistic simulations, J. Appl. Phys. 111, http://dx.doi.org/10.1063/1.3681321, URL https://aip.scitation.org/doi/10.1063/1.3681321.

[20] W.K. Kim, B.H. Kim, A molecular dynamics study on atomistic mechanisms of nano-scale cutting process of sapphire, J. Mech. Sci. Technol. (ISSN: 1976-3824) 31 (9) (2017) 4353–4362, http://dx.doi.org/10.1007/s12206-017-0834-5.

[21] W.K. Kim, D. Xi, B.H. Kim, Nanoscale indentation and scratching tests of single crystal sapphire using molecular dynamics simulation, Comput. Mater. Sci. (ISSN: 0927-0256) 170 (2019) 109195, http://dx.doi.org/10.1016/j.commatsci.2019.109195, URL https://www.sciencedirect.com/science/article/pii/S092702561930494X.

[22] J. Lin, F. Jiang, Q. Wen, Y. Wu, J. Lu, Z. Tian, N. Wang, Deformation anisotropy of nano-scratching on C-plane of sapphire: A molecular dynamics study and experiment, Appl. Surf. Sci. (ISSN: 0169-4332) 546 (2021) 149091, http://dx.doi.org/10.1016/j.apsusc.2021.149091, URL https://www.sciencedirect.com/science/article/pii/S0169433221001677.

[23] J. Lin, F. Jiang, X. Xu, J. Lu, Z. Tian, Q. Wen, X. Lu, Molecular dynamics simulation of nanoindentation on c-plane sapphire, Mech. Mater. (ISSN: 0167-6636) 154 (2021) 103716, http://dx.doi.org/10.1016/j.mechmat.2020.103716, URL https://www.sciencedirect.com/science/article/pii/S0167663620307420.

[24] E. Tochigi, B. Miao, A. Nakamura, N. Shibata, Y. Ikuhara, Atomic-scale mechanism of rhombohedral twinning in sapphire, Acta Mater. (ISSN: 1359-6454) 216 (2021) 117137, http://dx.doi.org/10.1016/j.actamat.2021.117137, URL https://www.sciencedirect.com/science/article/pii/S1359645421005176.

[25] T. Qiu, F. Jiang, N. Wang, J. Lin, Z. Tian, Y. Wu, Q. Wen, J. Lu, Atomistic understanding of the variable nano-hardness of C-plane sapphire considering the crystal anisotropy, J. Mater. Res. Technol. (ISSN: 2238-7854) 29 (2024) 4514–4525, http://dx.doi.org/10.1016/j.jmrt.2024.02.161, URL https://www.sciencedirect.com/science/article/pii/S2238785424004563.

[26] Q. Xu, A. Zaborowska, K. Mulewska, W. Huo, K. Karimi, F.J. Domínguez-Gutiérrez, Łukasz Kurpaska, M.J. Alava, S. Papanikolaou, Atomistic insights into nanoindentation-induced deformation of α-Al2O3 single crystals, Vacuum (ISSN: 0042-207X) 219 (2024) 112733, http://dx.doi.org/10.1016/j.vacuum.2023.112733, URL https://www.sciencedirect.com/science/article/pii/S0042207X23009302.

[27] A.H. Heuer, Deformation twinning in corundum, Philos. Mag.: J. Theor. Exp. Appl. Phys. 13 (122) (1966) 379–393, http://dx.doi.org/10.1080/14786436608212616.

[28] S.L. Korinek, J. Castaing, Slip and twinning in polycrystalline alumina (α-Al2O3) deformed under hydrostatic pressure between 600° and 1000° C, J. Am. Ceram. Soc. 86 (4) (2003) 566–573, http://dx.doi.org/10.1111/j.1151-2916.2003.tb03342.x, URL https://ceramics.onlinelibrary.wiley.com/doi/abs/10.1111/j.1151-2916.2003.tb03342.x.

[29] J. Castaing, A. He, K.P.D. Lagerlöf, A.H. Heuer, Deformation of sapphire (α-Al2O3) by basal slip and basal twinning below 700°C, Phil. Mag. 84 (11) (2004) 1113–1125, http://dx.doi.org/10.1080/14786430310001613183.

[30] K. Wang, F. Jiang, L. Yan, X. Xu, N. Wang, X. Zha, X. Lu, Q. Wen, Study on mechanism of crack propagation of sapphire single crystals of four different orientations under impact load and static load, Ceram. Int. (ISSN: 0272-8842) 45 (6) (2019) 7359–7375, http://dx.doi.org/10.1016/j.ceramint.2019.01.021, URL https://www.sciencedirect.com/science/article/pii/S0272884219300239.

[31] S. Huang, J. Lin, N. Wang, B. Guo, F. Jiang, Q. Wen, X. Lu, Fracture behavior of single-crystal Sapphire in different crystal orientations, Crystals (ISSN: 2073-4352) 11 (8) (2021) 930, http://dx.doi.org/10.3390/cryst11080930, URL https://www.mdpi.com/2073-4352/11/8/930.

[32] F. Jiang, X. Luan, N. Wang, X. Xu, X. Lu, Q. Wen, Research on the dynamic mechanical properties of C-plane sapphire under impact loading, Ceram. Int. (ISSN: 0272-8842) 44 (8) (2018) 9839–9847, http://dx.doi.org/10.1016/j.ceramint.2018.02.227, URL https://www.sciencedirect.com/science/article/pii/S0272884218305388.

[33] X. Luan, F. Jiang, W. Ningchang, X. Xu, X. Lu, Q. Wen, The mechanical response characteristics of Sapphire under dynamic and quasi-static indentation loading, Ceram. Int. 44 (13) (2018) 15208–15218, http://dx.doi.org/10.1016/j.ceramint.2018.05.162.

[34] F. Smidt, An analysis of thermally activated flow in α iron based on T–τ ∗ considerations, Acta Metall. (ISSN: 0001-6160) 17 (4) (1969) 381–392, http://dx.doi.org/10.1016/0001-6160(69)90018-2, URL https://www.sciencedirect.com/science/article/pii/0001616069900182.

[35] S. Plimpton, Fast parallel algorithms for short – range molecular dynamics, J. Comput. Phys. (ISSN: 00219991) 117 (1994) (1995) 1–19, URL http://lammps.sandia.gov.

[36] A. Kavalur, V. Guduguntla, W.K. Kim, Effects of Langevin friction and time steps in the molecular dynamics simulation of nanoindentation, Mol. Simul. 46 (12) (2020) 911–922, http://dx.doi.org/10.1080/08927022.2020.1791858.

[37] P. Vashishta, R.K. Kalia, A. Nakano, J.P. Rino, Interaction potentials for alumina and molecular dynamics simulations of amorphous and liquid alumina, J. Appl. Phys. 103 (8) (2008) 083504, http://dx.doi.org/10.1063/1.2901171.

[38] S.B. Kwon, A. Nagaraj, D. Xi, Y. Du, D.N. Kim, W.K. Kim, S. Min, Studying crack generation mechanism in single-crystal sapphire during ultra-precision machining by MD simulation-based slip/fracture activation model, Int. J. Precis. Eng. Manuf. 24 (5) (2023) 715–727, http://dx.doi.org/10.1007/s12541-023-00776-w.

[39] S.B. Kwon, A. Nagaraj, D.N. Kim, D. Xi, Y. Du, W.K. Kim, S. Min, Prediction of crack initiation in single-crystal sapphire during ultra-precision machining using MD simulation-based slip/fracture activation model, Precis. Eng. (ISSN: 0141-6359) 86 (2024) 265–275, http://dx.doi.org/10.1016/j.precisioneng.2023.12.007, URL https://www.sciencedirect.com/science/article/pii/S0141635923002349.

[40] A. Stukowski, Visualization and analysis of atomistic simulation data with OVITO–the Open Visualization Tool, Modelling Simul. Mater. Sci. Eng. 18 (1) (2009) 015012, http://dx.doi.org/10.1088/0965-0393/18/1/015012.

[41] G.A. Tomlinson, A molecular theory of friction, Phil. Mag. 7 (1929) 905–939.

[42] H. Kramers, Brownian motion in a field of force and the diffusion model of chemical reactions, Physica (ISSN: 0031-8914) 7 (4) (1940) 284–304, http://dx.doi.org/10.1016/S0031-8914(40)90098-2, URL https://www.sciencedirect.com/science/article/pii/S0031891440900982.

[43] J.R. Rice, G.E. Beltz, The activation energy for dislocation nucleation at a crack, J. Mech. Phys. Solids (ISSN: 0022-5096) 42 (2) (1994) 333–360, http://dx.doi.org/10.1016/0022-5096(94)90013-2, URL https://www.sciencedirect.com/science/article/pii/0022509694900132.

[44] E. Gnecco, R. Bennewitz, T. Gyalog, C. Loppacher, M. Bammerlin, E. Meyer, H.-J. Güntherodt, Velocity dependence of atomic friction, Phys. Rev. Lett. 84 (2000) 1172–1175.

[45] W.K. Kim, M.L. Falk, Role of intermediate states in low-velocity friction between amorphous surfaces, Phys. Rev. B (ISSN: 1098-0121) 84 (2011) 165422, http://dx.doi.org/10.1103/PhysRevB.84.165422.

[46] E.B. Tadmor, F. Legoll, W.K. Kim, L.M. Dupuy, R.E. Miller, Finite-temperature quasi-continuum, Appl. Mech. Rev. 65 (2013) 010803, http://dx.doi.org/10.1115/1.4023013.

[47] C.E. Maloney, D.J. Lacks, Energy barrier scalings in driven systems, Phys. Rev. E 73 (2006) 061106, http://dx.doi.org/10.1103/PhysRevE.73.061106, URL https://link.aps.org/doi/10.1103/PhysRevE.73.061106.

[48] M.L. Falk, J.S. Langer, Dynamics of viscoplastic deformation in amorphous solids, Phys. Rev. E 57 (1998) 7192–7205, http://dx.doi.org/10.1103/PhysRevE.57.7192, URL https://link.aps.org/doi/10.1103/PhysRevE.57.7192.